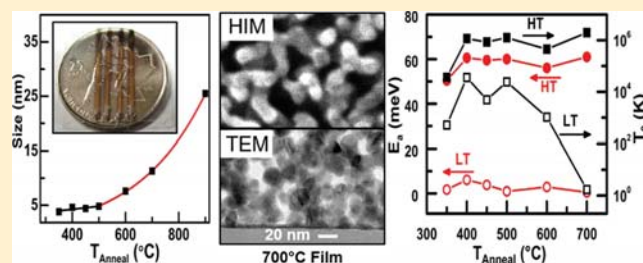


# Electronic Transport in Tin(IV) Oxide Nanocrystalline Films: Two-Medium Transport with Three-Dimensional Variable-Range Hopping Mechanism for the Ultrasmall Nanocrystallite Size Regime

Samad Bazargan, Nina F. Heinig, Jose Fernando Rios, and K. T. Leung\*

WATLab and Department of Chemistry, University of Waterloo, Waterloo, Ontario N2L 3G1, Canada

**ABSTRACT:** Homogeneous, nanocrystalline films of tin(IV) oxide with controllable crystalline grains in the ultrasmall size range of 4–12 nm have been prepared by using a simple method of spin-coating followed by annealing in oxygen at different postannealing temperatures ( $T_{\text{anneal}}$ ). These nanocrystalline films all exhibit a high optical transparency of 90–100% in the visible region with a band gap of  $3.71 \pm 0.05$ – $3.87 \pm 0.05$  eV compared to 3.6 eV for bulk  $\text{SnO}_2$ , indicating a high carrier density for all the TO films. The films obtained with  $T_{\text{anneal}} \geq 350$  °C, marking the onset of crystallization, are found to be conductive. The ac resistivity is measured as a function of temperature between 50 and 280 K for all the conductive films, and two distinct behaviors are observed between 50 and 90 K (LT) and 120–280 K (HT). The presence of two different media, i.e., the crystalline grains and the charge-depletion layer, can explain the observed resistivity behavior. The excellent fit of a parallel resistor model to the resistivity data for samples obtained with  $T_{\text{anneal}} = 350$ – $700$  °C further validates the presence of the two media, revealing energy barrier heights of  $48.0 \pm 0.4$ – $60.5 \pm 0.4$  meV for transport across the grain boundaries. The resistivity behavior in each medium is best described by the three-dimensional variable-range hopping (3D-VRH) model, given its excellent fit to the experimental data. On the basis of the resistivity results as analyzed within this model, we conclude that increasing  $T_{\text{anneal}}$  leads to a reduction in the carrier density as defect density decreases. The 3D-VRH fits to the resistivity in the LT region further reveal that above the onset of exponential growth at  $T_{\text{anneal}} = 500$  °C, a remarkable improvement in the charge transport occurs likely due to the observed enhanced crystallinity. Postannealing at different temperatures, therefore, has a direct effect on the extent of crystallization in the amorphous matrix and the size of the resulting nanocrystallites, both of which affect the defect density and transport channels, and can therefore be used to provide fine control on the resistivity of the nanocrystalline  $\text{SnO}_2$  film.



## 1. INTRODUCTION

Nanocrystalline films of tin(IV) oxide (TO) or tin dioxide, with crystallite sizes below 10 nm are of special interest because of their prominent gas sensing and catalytic properties.<sup>1,2</sup> The charge transport in nanocrystalline TO structures is complex and is different from bulk charge transport in several aspects. In bulk semiconducting TO films, conduction originates from n-type carriers, which have been proposed to be due to oxygen deficiencies, Sn interstitials, crystalline defects,<sup>3</sup> or hydrogen doping.<sup>4</sup> Moreover, different charge trap levels with different activation energies are observed in these films, depending on their synthesis methods. In the case of nanocrystalline films, the small size of the crystallites and their interconnections, as well as any gaseous species adsorbed on their large surface areas can further modify their charge transport properties. In particular, for nanocrystallites smaller than 10 nm, the radius of the nanocrystallite becomes comparable to the Debye length (calculated to be  $\sim 3$  nm for  $\text{SnO}_2$  at 250 °C)<sup>5</sup>, which corresponds to the approximate size of the charge-depletion layer created by an adsorbed species.<sup>6</sup> The comparable size of the charge depleted region to the size of the nanocrystallite and the significant surface-to-volume ratio in these films can result in drastic changes in the conduction

channel and in the charge transport through the nanocrystallites and their interconnections upon exposure to different gas species.<sup>1,7</sup> Depending on the size of the conduction channels relative to the mean free path of the carriers, charge carrier scattering effects can also be induced.<sup>6</sup>

In the present work, we investigate the electronic structure and transport properties of nanocrystalline TO films with crystallites in the 4–12 nm size range. Films with selected crystallite sizes are commonly obtained by first synthesizing nanoparticles in solution phase and then spin-coating the precipitated nanoparticles onto a substrate and are usually treated with postannealing in order to create connection between the nanoparticles.<sup>8,9</sup> However, an elaborate procedure is needed in the solution-phase chemistry to control the size of the nanoparticles, making fabrication of large-area nanocrystalline films with specific crystallite size difficult. In the present study, we prepare nanocrystalline films using a different method of controlling the crystallization of an amorphous TO phase by manipulating the postannealing

Received: October 13, 2011

Revised: December 5, 2011

Published: December 27, 2011

temperature ( $T_{\text{anneal}}$ ).<sup>10</sup> Nanocrystallites with controllable size below 12 nm can be easily obtained by keeping  $T_{\text{anneal}}$  close to the onset of crystallization. This method of fabrication involves fewer steps and is easily scalable and compatible with industrial processes. Optical and electronic transport measurements, in conjunction with extensive structural and compositional characterization, performed on the resulting TO films can provide a better understanding of their electronic properties. In particular, the optical transmittance of TO films with different nanocrystallite sizes and crystalline-to-amorphous phase ratios are measured in order to determine the effect of the amorphous phase and nanocrystallite size on the corresponding band gap energies and electronic structures. Furthermore, the effects of the nanocrystallite size and the presence of amorphous phase on the electrical conductivity are studied by measuring the ac resistivity of the films in the temperature range of 50–280 K, which can be understood using the thermal activation and variable range hopping models. Carrying out the electronic transport measurements at low temperature and in high vacuum helps to recover the conduction channels and reduces the adsorption/desorption rate of gases and their effects on the electronic transport. These measurements elucidate the nature of the charge carrier activation and transport through the different possible conduction channels. The information obtained through these measurements is of great interest to the application of these nanocrystalline TO films as gas sensors, catalysts, and transparent conducting active/passive layers.

## 2. EXPERIMENTAL DETAILS

Our group has recently developed a method of producing smooth, homogeneous nanocrystalline TO films. As illustrated schematically in Figure 1a, a 2 M solution of  $\text{SnCl}_4 \cdot 5\text{H}_2\text{O}$  in isopropanol is deposited onto a glass (Corning #0211) or quartz substrate by spin-coating at 1000–1800 rpm, followed by postannealing in a tube furnace at a selected temperature (250–900 °C) in flowing oxygen. Glass substrate is chosen for synthesizing nanocrystallites with average sizes below 5 nm, where  $T_{\text{anneal}}$  is limited to the annealing point of Corning #0211 glass (550 °C). However, for studying the effect of increasing the nanocrystallite sizes to 12 nm (obtained with a higher  $T_{\text{anneal}}$ ) on the optical and transport properties, quartz substrate is used for  $T_{\text{anneal}} = 600$  and 700 °C. It should be noted that the TO films deposited on quartz for  $T_{\text{anneal}} < 550$  °C show chemical and crystalline features similar to those obtained on the glass substrates. The TO films so obtained are found to be generally smooth with a granular morphology with a thickness of  $270 \pm 50$  nm (Figure 1c–f). The thickness can be further controlled by changing the concentration of the precursor solution, and the reported variance of 50 nm is an estimate of the observed differences in the thickness of the deposited layer in several separate depositions. X-ray diffraction (XRD) studies on the TO films obtained with  $T_{\text{anneal}} = 200$ –700 °C are performed by using a PANalytical MRD X'pert Pro XRD system in the glancing-incidence mode with an incidence angle of 0.3°. Surface morphology and the local crystalline structures of the films are examined by using a LEO FESEM 1530 scanning electron microscope (SEM) and a Zeiss Orion Plus helium ion microscope (HIM), and a JEOL 2010F transmission electron microscope (TEM) operating at 200 kV, respectively. UV–visible transmission spectra for TO films are recorded by using a Perkin-Elmer Lambda 35 UV–vis spectrometer equipped with a Labsphere

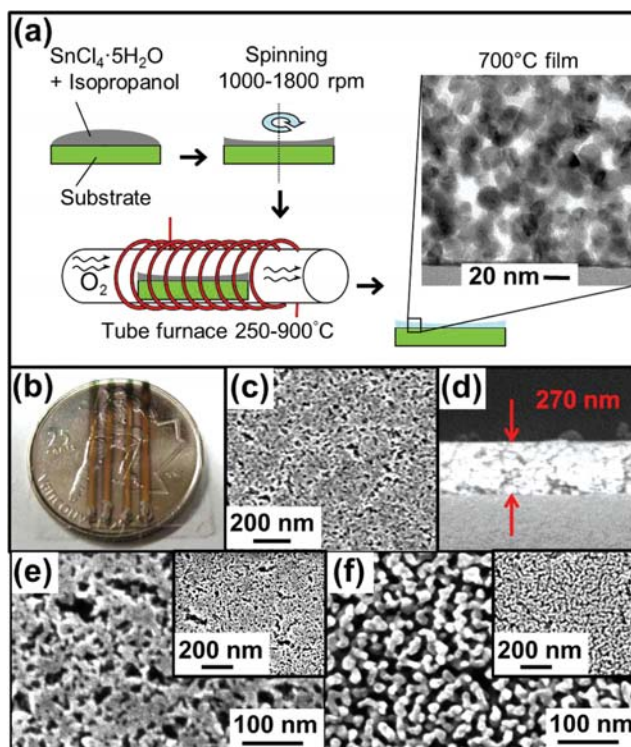


**Figure 1.** (a) Schematics of the synthesis method of nanocrystalline  $\text{SnO}_2$  films (Reprinted with permission from ref 10. Copyright 2010 American Chemical Society.) with a TEM cross-sectional image depicting the granular structure of a film obtained with postannealing at 700 °C. (b) Photograph of a typical film prepared on a glass substrate, illustrating the transparency of the film and the four gold stripes deposited as contacts for the four-point probe resistivity measurement. (c and d) SEM images depicting the top and side views of the granular structure of the film obtained with postannealing at 400 °C on glass. (e and f) High-magnification helium ion microscopy (HIM) images of films obtained on glass and quartz with postannealing at 400 °C and at 700 °C, respectively, with the corresponding low-magnification images shown as insets.

integrating sphere. Details of the preparation and characterization of these TO films have been discussed elsewhere.<sup>10</sup>

The ac conductivity of these nanocrystalline films is measured as a function of temperature by a four-point probe method. With the TO film covering the entire substrate ( $20 \times 20 \text{ mm}^2$ ), four gold strips (each 0.8 mm wide) are deposited as voltage/current contacts 2 mm apart on the TO film, and they are connected to the measurement wires using silver paste (Figure 1b). After curing the silver paste by illumination under an incandescent light for 12 h, the sample is then transferred to a cryopump station and evacuated to an initial vacuum of  $1 \times 10^{-5}$  mbar. To decrease the amount of adsorbed gases on the surface in order to reduce their effect on the resistivity, as known to occur for TO films,<sup>11</sup> and to recover the conduction channels, all the samples are retained in vacuum for at least 24 h before measurement. A Stanford Research Systems 510 lock-in amplifier with a 1 Hz internal oscillator source operating at 1 V through a 10 M $\Omega$  current-limiting resistor is used to measure the ac resistivity of the samples. The ac results are also compared with dc resistivity data taken at 1  $\mu\text{A}$  with a monitored constant current source in order to ensure the reproducibility of the observed temperature behavior of the ac resistivity.



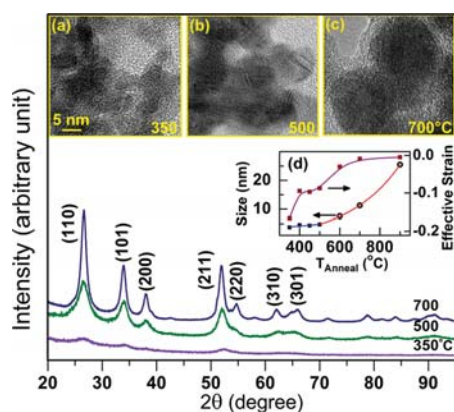


**Figure 2.** Typical glancing-incidence X-ray diffraction patterns of SnO<sub>2</sub> films prepared with postannealing temperatures ( $T_{\text{anneal}}$ ) of 350 and 500 °C on glass substrates and of 700 °C on a quartz substrate, where glass and quartz substrates are used for films obtained with  $T_{\text{anneal}} = 350, 400, 450, \text{ and } 500$  °C and of 600, 700, and 900 °C, respectively. Typical TEM images for the samples obtained with  $T_{\text{anneal}} =$  (inset a) 350 °C, (inset b) 500 °C, and (inset c) 700 °C are shown with the same scale. Inset d shows the change in the crystallite size and effective strain with increasing  $T_{\text{anneal}}$ , with the size data points in the 350–500 °C range fitted by a straight line, and those in the 500–900 °C range are fitted by an exponential curve. The line connecting the effective strain data points is merely for guiding the eye.

### 3. RESULTS AND DISCUSSION

In our previous work, we demonstrated that the size of the nanocrystallites in a thin spin-coated TO film ( $270 \pm 50$  nm thick) can be easily controlled over the 4–25 nm size range by manipulating  $T_{\text{anneal}}$ .<sup>10</sup> In particular, XRD studies of TO films obtained at different  $T_{\text{anneal}}$ s show an onset of crystallization at 350 °C (Figure 2). The corresponding crystallite sizes are estimated by applying the Debye–Scherrer analysis to the broadening of the (110) peak and are found to be in good agreement with the average nanocrystallite sizes estimated from TEM measurement (shown in Figure 2, inset a–c). The effective strain of the nanocrystallites is also estimated from the broadening of the (110), (101), and (200) peaks by using the Williamson–Hall plot,<sup>12</sup> ( $B \cos \theta$ )/ $\lambda = K/D + (e \sin \theta)/\lambda$ , where  $B$  is the total broadening after correcting for the instrumental broadening (0.40°),  $\theta$  is the peak position in radian,  $\lambda$  is the X-ray wavelength,  $K$  is the shape factor (0.89 for spherical grains),  $D$  is the crystallite size, and  $e$  is the effective strain. Both the XRD and TEM results confirm the presence of a single SnO<sub>2</sub> phase in these TO films. As shown in Figure 2, inset d, the nanocrystallite size remains in the 4–5 nm range for  $T_{\text{anneal}} = 350\text{--}500$  °C, which is likely due to the presence of strain on the particles from the amorphous phase limiting the growth of crystallites beyond this size limit.<sup>10</sup> For  $T_{\text{anneal}} > 500$  °C, the nanocrystalline strain starts to decrease rapidly, and the resulting exponential increase in nanocrystallite size with increasing temperature suggests an Arrhenius-like growth mechanism.

Figure 3 shows the UV–visible transmission spectra of the TO films obtained with  $T_{\text{anneal}} = 350\text{--}500$  °C on glass and with  $T_{\text{anneal}} = 550\text{--}700$  °C on quartz substrates. Evidently, these films all exhibit a high optical transparency of 90–100% in the visible region (1.2–3.5 eV). The absorption edges for films obtained with  $T_{\text{anneal}}$  at and below 500 °C are found to be very close to that of the glass substrate (Figure 3a), while those obtained with

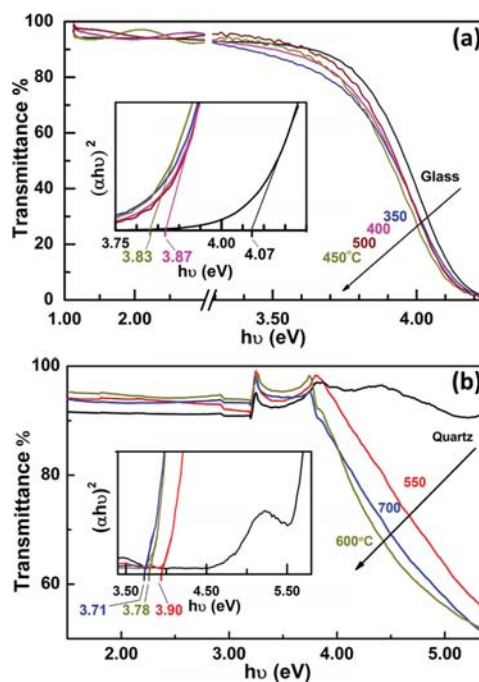


**Figure 3.** UV–visible spectra of the SnO<sub>2</sub> films prepared with different postannealing temperatures (a) of 350–500 °C on glass and (b) of 550–700 °C on quartz substrates. Insets show the  $(ah\nu)^2$  versus  $h\nu$  plots illustrating the method of estimating the band gap.

$T_{\text{anneal}}$  above 500 °C show a distinctly different absorption edge from the quartz substrate (Figure 3b). From the absorption coefficient given by the Beer–Lambert law,  $\alpha = \ln(I)/d$ , where  $I$  is the transmittance, and  $d$  is the optical path length, we calculate the band gap  $E_g$  using the Tauc equation for absorption in a direct-band gap material:  $ah\nu = A(h\nu - E_g)^{1/2}$ , where  $A$  is a constant, and  $h\nu$  is the incident photon energy.<sup>13–15</sup> Insets of Figure 3 show the corresponding plots of  $(ah\nu)^2$  versus  $h\nu$  for the TO films obtained on the glass and quartz substrates in which the zero-crossing of the tangent to the curve provides an estimate of the band gap of the respective sample. The band gap values so determined for all the TO films on glass are clearly different from the estimated band gap value of  $4.07 \pm 0.05$  eV for the glass substrate. This difference is not due to scattering from the additional TO films because the samples exhibit essentially the same high transmittance in the visible region as the pristine glass substrate. The estimated band gap values for the TO films obtained with  $T_{\text{anneal}} = 350\text{--}500$  °C are found to be  $3.83 \pm 0.05\text{--}3.87 \pm 0.05$  eV, indicating that these crystalline samples obtained with  $T_{\text{anneal}} = 350\text{--}500$  °C (Figure 2, inset d) have similar energy band structures. Crystallization of the samples at 350–500 °C, therefore, has not led to any detectable change in the band structure. The band gap values estimated for samples obtained on quartz with higher  $T_{\text{anneal}}$  of 550, 600, and 700 °C are  $3.90 \pm 0.05, 3.78 \pm 0.05, \text{ and } 3.71 \pm 0.05$  eV, respectively. It should be noted that the band gap value for TO film obtained with  $T_{\text{anneal}} = 550$  °C on quartz (Figure 3b) is essentially the same as those obtained with  $T_{\text{anneal}} \leq 500$  °C on glass (Figure 3a). For the TO films deposited on quartz, their band gap values follow a discernible decreasing trend with increasing  $T_{\text{anneal}}$  above 550 °C (Figure 3b, inset). Furthermore, the estimated band gap values for all the TO films (obtained with  $T_{\text{anneal}} = 350\text{--}700$  °C) are found to be

higher than the reported value for single-crystalline SnO<sub>2</sub> (3.6 eV).<sup>7,16</sup> The conduction band in the electronic structure of TO is composed of the 5s orbitals of Sn and has a strongly dispersive s-type shape.<sup>7,17</sup> The observed blue shift in the band gap can, therefore, be explained by the Moss–Burstein effect, where increased n-doping due to a large number of defects in the crystal fills more conduction band states, leading to an increase in the measured optical band gap. Similar blue shifts have also been found for In<sub>2</sub>O<sub>3</sub>, ZnO, CdO, and other transparent conducting oxides.<sup>7,18</sup> Our optical transmission measurement, therefore, indicates that even the nanocrystalline films obtained with a high  $T_{\text{anneal}}$  (550–700 °C) that show a high degree of crystallinity still have a high carrier density.

The ac resistivity results for TO films obtained with  $T_{\text{anneal}} = 350$ –700 °C in the temperature range of 50–280 K are shown

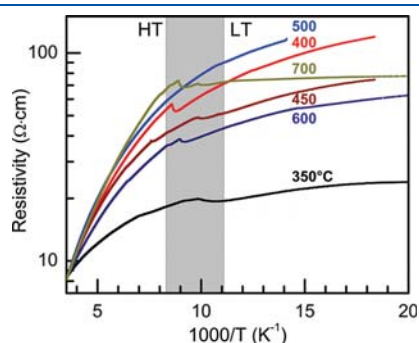


**Figure 4.** Resistivity of the SnO<sub>2</sub> films prepared with postannealing at 350–700 °C in the 50–280 K range. To better illustrate the change in their behavior, the resistivity curves are normalized to the resistivity value at 280 K of the sample obtained with postannealing at 350 °C, only for presentation purpose. Gray area marks the intermediate region (90–120 K) between the HT (120–280 K) and LT (50–90 K) regions.

in Figure 4. In order to check the reproducibility of the observed resistivity behavior with temperature, dc measurement is also performed on the films obtained with  $T_{\text{anneal}} = 400, 450,$  and 600 °C. The similar dc resistivity behavior so observed confirms the ac resistivity result. In spite of our best effort to decrease the gas exchange rates on the surface of the samples by keeping the samples in vacuum for at least 24 h before the measurement, the repeated cooling and heating cycles in between our resistivity measurements could still cause a general variation of 40 Ω·cm in the room-temperature resistivity values. This behavior is due to the small size of the crystalline grains and the high sensitivity of these highly resistive pristine films to the amount of adsorbed gases, which lead to the exceptional gas sensing properties of SnO<sub>2</sub>. Similar variation in resistivity due to gas adsorption has also been reported to occur for TO films.<sup>11,19,20</sup> In order to better present the changes in the resistivity behavior for all the samples, the resistivity curves plotted in Figure 4 are normalized to the resistivity value at 280 K of the sample obtained with  $T_{\text{anneal}} = 350$  °C (8.5 Ω·cm). All the analysis is done with the raw data and not with the normalized data shown in Figure 4. The films obtained with  $T_{\text{anneal}} < 350$  °C are found to be amorphous and not conductive. The amorphous phase that is present with particularly high volumetric percentage in the samples obtained with low  $T_{\text{anneal}}$  of 350–500 °C will, therefore, not contribute to the conductivity of these samples. Evidently, for the films obtained with  $T_{\text{anneal}} \geq 350$  °C (shown in Figure 4), nearly linear conduction trends over 120–280 K (denoted as high-temperature or HT region) and below 90 K (denoted as low-temperature or LT region) are observed, along with an intermediate region with complex behavior at 90–120 K (marked as a gray area in Figure 4). Moreover, for all the films, there is a decrease in the tangential slope of the curve in going from the HT region to the LT region.

In order to examine the underlying conduction mechanism, we fit the resistivity data to different electronic transport models involving

**Table 1.**<sup>a</sup>

$T_{\text{anneal}}$ (°C)	$\rho$ at 280 K (Ω·cm)	HT/ LT regions (K)	thermal activation		variable-range hopping		
			$E_a^0$ (meV) [R <sup>2</sup> ]	$E_a^{\text{SE}}$ (meV) [adj. R <sup>2</sup> ]	CG		
					$T_0$ (K) [R <sup>2</sup> ]	2D	3D
			HT/LT	HT/LT	HT/LT	HT/LT	HT/LT
350	8.5	296–114/92–51	14.6 ± 0.1 [0.9591]/	50.4 ± 0.3/	643 [0.9799]/	4.1 × 10 <sup>3</sup> [0.9852]/	3.6 × 10 <sup>4</sup> [0.9876]/
			2.44 ± 0.03 [0.9693]	1.72 ± 0.02 [0.9972]	47 [0.9803]	131 [0.9833]	514 [0.9847]
400	4.0	297–116/ 113–54	35.0 ± 0.1 [0.9804]/	60.6 ± 0.3/	3.6 × 10 <sup>3</sup> [0.9936]/	5.5 × 10 <sup>4</sup> [0.9964]/	1.2 × 10 <sup>6</sup> [0.9975]/
			7.7 ± 0.1 [0.9713]	6.12 ± 0.03 [0.9983]	419 [0.9851]	3.3 × 10 <sup>3</sup> [0.9887]	3.6 × 10 <sup>4</sup> [0.9903]
450	51.6	296–131/94–49	34.2 ± 0.2 [0.9767]/	59.5 ± 0.2/	3.3 × 10 <sup>3</sup> [0.9902]/	4.5 × 10 <sup>4</sup> [0.9934]/	8.6 × 10 <sup>5</sup> [0.9947]/
			4.2 ± 0.1 [0.9626]	3.82 ± 0.02 [0.9990]	144 [0.9767]	711 [0.9807]	4.9 × 10 <sup>3</sup> [0.9825]
500	28.9	288–111/89–70	34.5 ± 0.2 [0.9685]/	48.1 ± 0.4/	3.2 × 10 <sup>3</sup> [0.9791]/	4.8 × 10 <sup>4</sup> [0.9854]/	1.0 × 10 <sup>6</sup> [0.9882]/
			7.13 ± 0.01 [0.9956]	0.10 ± 0.08 [0.9922]	346 [0.9972]	2.4 × 10 <sup>3</sup> [0.9977]	2.4 × 10 <sup>4</sup> [0.9979]
600	2.6	299–121/84–31	28.4 ± 0.1 [0.9802]/	56.1 ± 0.3/	2.3 × 10 <sup>3</sup> [0.9934]/	2.7 × 10 <sup>4</sup> [0.9962]/	4.5 × 10 <sup>5</sup> [0.9973]/
			2.23 ± 0.02 [0.9794]	4.25 ± 0.05 [0.9988]	56.5 [0.9910]	205 [0.9935]	1.0 × 10 <sup>3</sup> [0.9945]
700	9.9	296–124/88–28	41.6 ± 0.1 [0.9898]/	61.0 ± 0.4/	4.6 × 10 <sup>3</sup> [0.9946]/	7.7 × 10 <sup>4</sup> [0.9971]/	1.8 × 10 <sup>6</sup> [0.9980]/
			0.43 ± 0.01 [0.9892]	0.52 ± 0.01 [0.9937]	2.2 [0.9885]	1.7 [0.9868]	1.7 [0.9856]

<sup>a</sup> Room-temperature resistivity ( $\rho$  at 280 K) for TO films obtained with different postannealing temperatures ( $T_{\text{anneal}}$ ); activation energies in the thermal activation model:  $E_a^0$  obtained by fitting the data in the high-temperature (HT) and low-temperature (LT) regions separately, and  $E_a^{\text{SE}}$  obtained by fitting the data over the full temperature range using the parallel resistor model (eq 3); and  $T_0$  values in the variable-range hopping models obtained by fitting the resistivity data in the specified HT and LT regions. The coefficients of determination,  $R^2$ , are given in square parentheses (For  $E_a^{\text{SE}}$  values of the two-medium model, adjusted  $R^2$  values are listed).

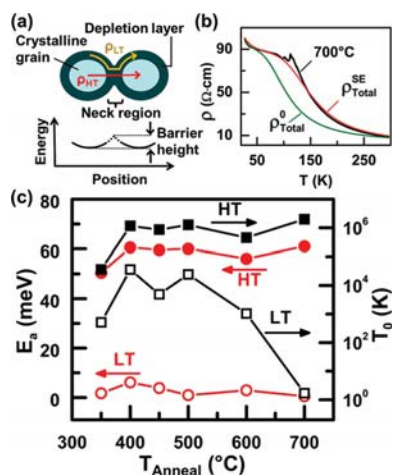


**Figure 5.** (a) Schematic representation of the two-medium model for electronic transport through the neck region of two adjoining crystalline grains (medium one), with a potential barrier, and through the depletion layer (medium two). (b) Comparison of the resistivity data of the sample obtained with postannealing at 700 °C with the  $\rho_{\text{total}}^0$  curve calculated by treating the independently obtained low-temperature (LT) resistivity  $\rho_{\text{LT}}^0$  and high-temperature (HT) resistivity  $\rho_{\text{HT}}^0$  in parallel, and with the  $\rho_{\text{total}}^{\text{SE}}$  curve obtained by fitting iteratively to the parallel resistor model with  $\rho_{\text{LT}}^0$  and  $\rho_{\text{HT}}^0$  as the initial values. (c)  $T_0$  parameter, obtained from fitting the 3D-variable-range hopping model to the resistivity data in the HT and LT regions, and the  $E_a^{\text{SE}}$  values, obtained for the HT and LT regions by fitting the resistivity data over the entire temperature range using the parallel resistor model, plotted as a function of the postannealing temperature,  $T_{\text{anneal}}$ , as indicated in Table 1.

the thermal activation and variable-range hopping (VRH) mechanisms, both of which have been extensively used to describe the transport in semiconducting nanostructures including CdSe nanocrystals,<sup>21</sup> belt-shaped monocrystals<sup>22</sup> and nanowires<sup>23</sup> of SnO<sub>2</sub>, and thin films of In<sub>2</sub>O<sub>3</sub>.<sup>24</sup> In the thermal activation model, the resistivity,  $\rho$ , is given as a function of temperature,  $T$ , by

$$\rho(T) = \rho_0 \exp\left(\frac{E_a}{k_B T}\right) \quad (1)$$

where  $E_a$  is the activation energy of carriers,  $k_B$  is the Boltzmann constant, and  $\rho_0$  is the pre-exponential factor. The corresponding relationship used for the VRH mechanisms is

$$\rho(T) = \rho_0 \exp\left[\left(\frac{T_0}{T}\right)^{1/n+1}\right] \quad (2)$$

where  $n = 1, 2$ , and  $3$  for the Efros–Shklovskii or Coulomb Gap (CG), two-dimensional (2D), and three-dimensional (3D) transport models, respectively, and  $\rho_0$  is the pre-exponential factor. The  $T_0$  parameter is related to the density of states at the Fermi level,  $g_f$ , and the carrier localization length,  $a$ , by  $T_0 = (\beta_{\text{CG}} e^2) / (k_B \kappa a)$ ,  $(\beta_{2D}) / (k_B g_f a^2)$ , and  $(\beta_{3D}) / (k_B g_f a^3)$ , for the CG-, 2D-, and 3D-VRH models, respectively, where  $\kappa$  is the dielectric constant, and  $\beta$  is obtained from Monte Carlo simulation (with  $\beta_{\text{CG}} = 2.8$ ,  $\beta_{2D} = 13.8$ , and  $\beta_{3D} = 21.2$ ).<sup>8,25</sup> The results for  $E_a$  and  $T_0$  obtained by fitting the resistivity data in the LT and HT regions for the samples obtained with different  $T_{\text{anneal}}$ s are presented in Table 1. The near-unity values for the coefficient of determination,  $R^2$ , obtained for these models indicate that the experimental data can be interpreted satisfactorily in both the thermal activation and VRH models. However, the

3D-VRH model gives the best fit to the data, suggesting that the electronic transport in these films is best described in terms of three-dimensional carrier hopping. This, therefore, shows that conduction is not restricted to lower dimensions, in contrast to that reported for films less than 100 nm thick,<sup>26,27</sup> because of the three-dimensional conduction network of nanocrystallites distributed in the entire thickness of the thicker ( $270 \pm 50$  nm) TO film (Figure 1d).<sup>10</sup>

The observed decrease in the tangential slope of the resistivity curve in going from the HT to LT region and the complex behavior in the intermediate region (90–120 K) can be explained by considering a two-medium resistance network model schematically shown in Figure 5a. Because of the presence of chemisorbed oxygen, a charge-depletion layer forms around the surfaces of and in the grain boundaries between the nanocrystallites. This layer also extends over the interconnecting neck when the nanocrystalline grain size is comparable to twice the Debye length,<sup>28</sup> resulting in a potential barrier ( $\phi_b$ ) for electronic transport through the grains (i.e., across the grain boundaries). Although the carrier concentration in the charge-depletion layer is lower than that in the grain by an exponential factor of  $\exp(-\phi_b / (k_B T))$ , charge transport through this layer could still contribute to the conductivity of these highly resistive nanocrystalline TO films especially for  $T < 100$  K, i.e., in the LT region (Figure 4). In the thermal activation model, two  $E_a$  values are found for the films obtained with  $T_{\text{anneal}} = 350$ – $700$  °C, by fitting their corresponding resistivity data in the LT and HT regions. The values so obtained for the LT region ( $0.43 \pm 0.01$ – $7.7 \pm 0.1$  meV) are considerably lower than those obtained in the HT region ( $14.6 \pm 0.1$ – $41.6 \pm 0.1$  meV) (Table 1). The difference in the  $E_a$  values observed in the HT and LT regions supports the presence of a potential barrier for transport across the grain boundaries, which becomes apparent in the HT region but not in the LT region. Electronic transport in inhomogeneous medium can be modeled by considering the appropriate series and/or parallel contributions of each region to the collective behavior, as discussed by Orton et al.<sup>28</sup> in interpreting the Hall effect results in various materials. In order to demonstrate that the two-medium model can account for the observed resistivity behavior of the TO films, we adopt a parallel resistor model as equivalent circuit for this two-medium structure, where the predominant resistivity in the HT region associated with transport through the grains and across the grain boundaries is represented by  $\rho_{\text{HT}}$ , and the predominant resistivity in the LT region related to transport through the charge-depletion layer is denoted by  $\rho_{\text{LT}}$ . The total resistivity of two parallel resistors ( $\rho_{\text{LT}}$  and  $\rho_{\text{HT}}$ ) is given by

$$\rho_{\text{total}} = \frac{\rho_{\text{HT}} \rho_{\text{LT}}}{\rho_{\text{HT}} + \rho_{\text{LT}}} \quad (3)$$

As an example, we compare in Figure 5b two calculated resistivity curves to the experimental resistivity curve for the sample obtained with  $T_{\text{anneal}} = 700$  °C, which is chosen because it exhibits a more dramatic difference in the  $E_a$  values and is, therefore, easier to discern the quality of fit (Table 1). By using the resistivity values obtained by fitting the data in the LT ( $\rho_{\text{LT}}^0$ ) and HT regions ( $\rho_{\text{HT}}^0$ ) independently, we calculate the corresponding  $\rho_{\text{total}}^0$  according to eq 3. Although this independent parallel resistor model gives qualitative agreement in the higher HT and lower LT regions and in providing a parallel trend with the experimental curve, there is obvious discrepancy. To correct for the discrepancy, which clearly originates from assuming the



independent resistivity behaviors in the LT and HT regions, we recalculate the total resistivity  $\rho_{\text{total}}^{\text{SE}}$  by fitting the data over the entire temperature range (280–50 K) iteratively with eq 3 to generate new  $\rho_{\text{LT}}^{\text{SE}}$  and  $\rho_{\text{HT}}^{\text{SE}}$  with their corresponding  $E_a$  values as semiempirical (SE) fitting parameters. Evidently, excellent agreement between the calculated  $\rho_{\text{total}}^{\text{SE}}$  curves with the experimental data is obtained, despite the deviations introduced by the complex resistivity behavior in the intermediate region in the fitting process (Figure 5b). These calculations validate our hypothesis of two-medium electronic transport in the TO films.

The optimized  $E_a$  values obtained for the calculated  $\rho_{\text{total}}^{\text{SE}}$  curves for all the TO films are given in Table 1 and plotted as a function of  $T_{\text{anneal}}$  in Figure 5c. The  $E_a^{\text{SE}}$  values for the electronic transport dominant in the HT and LT regions are found to be  $48.1 \pm 0.4$ – $61.0 \pm 0.4$  meV and  $0.1 \pm 0.08$ – $6.12 \pm 0.03$  meV, respectively. The difference between the  $E_a^{\text{SE}}$  value for transport through the grains and across the grain boundaries,  $\rho_{\text{HT}}$ , and that through the charge-depletion layer,  $\rho_{\text{LT}}$ , for each sample corresponds to the potential barrier. The small variations in the  $E_a^{\text{SE}}$  difference ( $48.0 \pm 0.4$ – $60.5 \pm 0.4$  meV) suggest a potential barrier of similar magnitude for all the TO films regardless of the different  $T_{\text{anneal}}$ s employed. Such a potential barrier could be due to similar gas adsorption densities in the neck regions in all the TO films, which suggests that the neck sizes remain smaller than twice the Debye length in spite of the increase in the nanocrystallite size from 4 to 12 nm. The variation in the resistivity in the intermediate temperature region (90–120 K) can be explained by the presence of potential barriers with different heights due to the statistical distribution in the neck size. The statistical variation in the potential barrier height would lead to different onset temperatures for blocking the conduction channels at various grain boundaries, and electronic transport would continue through the remaining active conduction routes as long as the low percolation limit has not reached. These changes in the conduction routes could lead to the observed resistivity variation in the intermediate temperature region, where electronic transport through the crystalline grains is nearly comparable to that through the depletion layer.

The fitted results (Table 1) show that electronic transport in each medium follows the 3D-VRH mechanism. Figure 5c shows the corresponding  $T_0$  parameters obtained by fitting the resistivity data in the HT and LT regions (representing transport through the grains and through the depletion layer, respectively) for the TO films prepared with different  $T_{\text{anneal}}$ s. The  $T_0$  value of  $3.6 \times 10^4$  K for the sample obtained with  $T_{\text{anneal}} = 350$  °C rises sharply to  $1.2 \times 10^6$  K when  $T_{\text{anneal}}$  is increased to 400 °C and stays almost unchanged with increasing  $T_{\text{anneal}}$  above 400 °C (Figure 5c). As  $T_0$  is inversely proportional to the density of states at the Fermi edge ( $g_f$ ) and the carrier localization length ( $a$ ), it is not surprising that its value has been reported to vary significantly for different materials, including  $1.1 \times 10^9$  K for belt-shape monocrystals of  $\text{SnO}_2$ ,<sup>22</sup>  $4.3 \times 10^7$  K for CdSe quantum dots,<sup>8</sup> and  $7.7 \times 10^3$  K for F-doped thin films of  $\text{SnO}_2$ .<sup>29</sup> In accord with our TEM and XRD results (Figure 2) that show improved crystallinity with increasing  $T_{\text{anneal}}$ , the carrier localization length does not decrease with increasing  $T_{\text{anneal}}$ . It can therefore be concluded that the observed increase of nearly 2 orders of magnitude in  $T_0$  with increasing  $T_{\text{anneal}}$  from 350 to 400 °C in the HT region is due to a sharp decrease in the carrier density at the Fermi edge. This is also in agreement with the results reported by Li et al.,<sup>17</sup> which correlate the carrier density at the Fermi edge with the density of oxygen vacancies as one of the common point defects in the crystal structure of TO. The

nearly unchanged  $T_0$  value with further increasing  $T_{\text{anneal}}$  to 700 °C suggests that the density of states at the Fermi energy is almost constant for samples prepared with postannealing above 400 °C. Moreover, in the LT region, we observe a rise in  $T_0$  value with increasing  $T_{\text{anneal}}$  from 350 to 400 °C, which can be explained by the high carrier density of the sample obtained with  $T_{\text{anneal}} = 350$  °C (similar to that for the HT region). The  $T_0$  value stays fairly stable for samples obtained with  $T_{\text{anneal}} = 400$ – $500$  °C and then starts to drop for the sample obtained with  $T_{\text{anneal}} = 600$  °C. For the sample obtained with  $T_{\text{anneal}} = 700$  °C, this decreasing trend reaches a dramatic reduction of almost four-orders of magnitude in  $T_0$ , compared to that obtained for samples with  $T_{\text{anneal}} = 400$ – $500$  °C. Since the density of states at the Fermi edge is not increasing, as suggested by the observed red shift in the band gap of the samples obtained with  $T_{\text{anneal}} = 600$  and 700 °C according to the optical measurement and also by the TEM and XRD results, this sharp drop in  $T_0$  indicates a correspondingly steep increase in the localization length for the samples obtained with  $T_{\text{anneal}} = 600$  and 700 °C. This increase in the localization length suggests that in the Arrhenius growth regime, overcoming the crystalline growth barrier improves the crystallinity of these films, the interconnections among the nanocrystallites, and also drastically reduces the grain boundary scattering effects.

#### 4. CONCLUSIONS

In summary, we study the optical and electronic transport properties of tin(IV) oxide nanocrystalline films prepared by a simple spin-coating/postannealing method. These TO films are found to consist of nanocrystallites in the 4–12 nm size range in an amorphous-phase matrix. These TO films are highly transparent in the visible region with discernibly larger band gaps of  $3.71 \pm 0.05$ – $3.87 \pm 0.05$  eV than bulk  $\text{SnO}_2$ , likely due to the Moss–Burstein effect, indicative of the high carrier densities in these TO films. The formation of the nanocrystalline phase above  $T_{\text{anneal}} = 350$  °C leads to a conducting film, with two distinct resistivity behaviors between 50 and 90 K (LT), and 120–280 K (HT). The 3D variable-range hopping model provides the best fit to the measured resistivity in the HT and LT regions. The different resistivity behaviors observed in the LT and HT regions can be explained by the two-medium model that takes into account electronic transport through the grains and across the grain boundaries with high carrier densities and through the depletion layer with very low carrier densities. This transport picture is supported by the excellent fit of our experimental data by the parallel resistor model. The energy corresponding to the potential barrier heights so obtained for transport through the grain boundaries for samples with  $T_{\text{anneal}} = 350$ – $700$  °C is found to be  $48.1 \pm 0.04$ – $61.0 \pm 0.4$  meV. Moreover, the variation in the resistivity in the intermediate temperature region (90–120 K) can be explained by the change in the aforementioned conduction routes due to existing distribution in the potential barrier heights between the grains. According to the 3D-VRH model, the observed trend in the  $T_0$  value in the HT region shows that the carrier density in the crystalline grains for the TO film obtained with  $T_{\text{anneal}} = 350$  °C is reduced upon increasing  $T_{\text{anneal}}$  to 400 °C and becomes nearly constant above 400 °C. The decreasing  $T_0$  trend for the LT region shows that increasing  $T_{\text{anneal}}$  above 500 °C leads to an increase in the localization length of the carriers, indicating a pronounced improvement in the crystallinity, interconnections, and the

conduction channels in the exponential growth regime. These results provide insights to the energy band structure and further elucidate the carrier transport in this network of TO nanocrystallites. These electronic transport properties depend on the nanocrystallite size, which can be effectively controlled by manipulating the postannealing temperature. In addition to the fundamental scientific interest, this information is crucial to potential applications of these nanocrystalline TO films in different areas including gas sensing, catalysis, and transparent conductive oxide materials.

## AUTHOR INFORMATION

### Corresponding Author

\*E-mail: tong@uwaterloo.ca.

## ACKNOWLEDGMENT

The present work was supported by the Natural Sciences and Engineering Research Council of Canada.

## REFERENCES

- (1) Seal, S.; Shukla, S. *JOM* **2002**, *54*, 35–38.
- (2) Yamazoe, N. *Sens. Actuators, B* **1991**, *5*, 7–19.
- (3) Kiliç, C.; Zunger, A. *Phys. Rev. Lett.* **2002**, *88*, 095501.
- (4) Singh, A. K.; Janotti, A.; Scheffler, M.; Van de Walle, C. G. *Phys. Rev. Lett.* **2008**, *101*, 1–4.
- (5) Ogawa, H.; Nishikawa, M.; Abe, A. *J. Appl. Phys.* **1982**, *53*, 4448–4455.
- (6) Barsan, N.; Weimar, U. *J. Electroceram.* **2001**, *7*, 143–167.
- (7) Batzill, M.; Diebold, U. *Prog. Surf. Sci.* **2005**, *79*, 47–154.
- (8) Liu, H.; Pourret, A.; Guyot-Sionnest, P. *ACS Nano* **2010**, *4*, 5211–5216.
- (9) Dave, N.; Pautler, B. G.; Farvid, S. S.; Radovanovic, P. V. *Nanotechnology* **2010**, *21*, 134023.
- (10) Bazargan, S.; Heinig, N. F.; Pradhan, D.; Leung, K. T. *Cryst. Growth Des.* **2011**, *11*, 247–255.
- (11) Kissine, V.; Sysoev, V. V.; Voroshilov, S. A. *Sens. Actuators, B* **2001**, *79*, 163–170.
- (12) Qadri, S. B.; Skelton, E. F.; Hsu, D.; Dinsmore, A. D.; Yang, J.; Gray, H. F.; Ratna, B. R. *Phys. Rev. B* **1999**, *60*, 9191–9193.
- (13) Gu, F.; Wang, S.; Lu, M. K.; Cheng, X. F.; Liu, S. W.; Zhou, G. J.; Xu, D.; Yuan, D. R. *J. Cryst. Growth* **2004**, *262*, 182–185.
- (14) Leite, E. R.; Bernardi, M. I. B.; Longo, E.; Varela, J. A.; Paskocimas, C. A. *Thin Solid Films* **2004**, *449*, 67–72.
- (15) Pradhan, D.; Leung, K. T. *Langmuir* **2008**, *24*, 9707–9716.
- (16) Ellmer, K. J. *Phys. D: Appl. Phys.* **2001**, *34*, 3097–3108.
- (17) Li, Z. Q.; Yin, Y. L.; Liu, X. D.; Li, L. Y.; Liu, H.; Song, Q. G. *J. Appl. Phys.* **2009**, *106*, 083701.
- (18) Moss, T. S. *Optical Properties of Semiconductors*, 2nd ed.; Butterworths: London, U.K., 1961.
- (19) Shanthi, E.; Banerjee, A.; Dutta, V.; Chopra, K. *Thin Solid Films* **1980**, *71*, 237–244.
- (20) Chopra, K. L.; Major, S.; Pandya, D. K. *Thin Solid Films* **1983**, *102*, 1–46.
- (21) Yu, D.; Wang, C.; Wehrenberg, B.; Guyot-Sionnest, P. *Phys. Rev. Lett.* **2004**, *92*, 1–4.
- (22) Lanfredi, A. J. C.; Geraldes, R. R.; Berengue, O. M.; Leite, E. R.; Chiquito, A. J. *J. Appl. Phys.* **2009**, *105*, 023708.
- (23) Ma, Y. J.; Zhou, F.; Lu, L.; Zhang, Z. *Solid State Commun.* **2004**, *130*, 313–316.
- (24) Rosenbaum, R. *Phys. Rev. B* **1991**, *44*, 3599–3603.
- (25) Shklovskii, B. I.; Efros, A. L. *Electronic Properties of Doped Semiconductors*; Springer: New York, 1984; Vol. 45.
- (26) Ivashchenko, A.; Kerner, I.; Kiosse, G.; Maronchuk, I. *Thin Solid Films* **1997**, *303*, 292–294.
- (27) Dominguez, J. E.; Fu, L.; Pan, X. Q. *Appl. Phys. Lett.* **2002**, *81*, 5168.
- (28) Orton, J. W.; Powell, M. J. *Rep. Prog. Phys.* **1980**, *43*, 1263–1307.
- (29) Subbaramaiah, K.; Sundararaja, V. *Appl. Surf. Sci.* **2006**, *253*, 1451–1458.